Aerospace Science and Technology 153 (2024) 109381

Contents lists available at ScienceDirect

Aerospace Science and Technology

journal homepage: www.elsevier.com/locate/aescte

Computational aeroacoustic study of co-rotating rotors in hover

Edoardo Grande [a,*], Shubham Shubham [b], Francesco Avallone [c], Daniele Ragni [a], Damiano Casalino [a]

[a] Delft University of Technology, Delft, 2629HS, the Netherlands
[b] Cranfield University, Bedford, MK43 0AL, United Kingdom
[c] Politecnico di Torino, Torino, 10129, Italy

ARTICLE INFO

Communicated by Kivanc Ekici

Keywords:
Co-rotating rotors
Aeroacoustics
LBM
PowerFLOW

ABSTRACT

This paper aims to investigate, by means of Lattice-Boltzmann simulations, the flow-field and far-field noise of two co-axial co-rotating rotors operating at 3000 rpm in hover conditions. The two co-rotating configurations are made by 2×2-bladed rotors with a fixed axial separation and two different azimuthal separations $\Delta\phi$ equal to 84° and 12°. Isolated 2- and 4-bladed rotors, are also simulated at the same operating conditions and used as aerodynamic and aeroacoustic reference. For both $\Delta\phi = 84°$ and 12°, the upper rotor tip vortices are accelerated downstream due to the induction from the lower rotor, avoiding blade vortex interaction (BVI). The lower rotor tip vortices convect into the wake with a lower velocity, causing BVI for $\Delta\phi = 12°$. The lower rotor shows a reduction of thrust, relative to the upper rotor, of 36% and 66% for $\Delta\phi = 84°$ and 12°, respectively. For $\Delta\phi = 12°$, the lower blades act as a wing flap for the upper ones, increasing their thrust. The tonal noise emission for the co-rotating rotors is driven by the interference between the acoustic waves from upper and lower rotors. Because of destructive interference, the configuration $\Delta\phi = 84°$ shows a first harmonic up to 15 dB lower than $\Delta\phi = 12°$, but still 4.5 dB higher than the isolated 4-bladed rotor.

1. Introduction

In the past few years, the development of unmanned aerial vehicles (UAVs), with various applications across military and civilian fields, and personal aerial vehicles (PAVs), for rapid mobility of people, has seen rapid growth. The different concepts proposed so far have in common the type of propulsion system, constituted by isolated or distributed propellers, which offer the capabilities of vertical take-off, landing and hovering. Since these vehicles are expected to be operated in close proximity to densely populated areas, including urban areas, their noise footprint will become a certification requirement [16].

To address both noise and aerodynamic requirements, unconventional configurations like co-axial co-rotating rotors must be explored. They are characterized by two rotors, connected to the same shaft, rotating in the same direction. They offer flexibility in adjusting the axial distance Δx between the rotors and the azimuthal separation $\Delta\phi$ between the propeller blades (also known as the phase or index angle). This design flexibility plays a crucial role in optimizing aerodynamic efficiency and reducing noise emissions, potentially surpassing the performance of isolated rotor configurations.

Several authors investigated the effect of the azimuthal separation on aerodynamic performance and sound pressure levels. Jacobellis et al. [18] observed a total thrust decrease by 10% as the azimuthal separation reached 0°. Landgrebe and Bellinger [20] carried out experiments with a small scale 2×3-bladed co-rotating rotor in hover and showed that, with azimuthal separations of 30° and 45°, improvements in thrust when compared to a co-planar configuration can be obtained. Rorke [27], by testing a full-scale co-rotating rotor in hover with 4 different azimuthal separations of 25.2°, 34.4°, 43.6° and 62.1°, measured 4 dB noise reduction at the first BPF for the 43.6° configuration and 6.1% thrust increase for 34.4° configuration. The latter was achieved by setting a differential collective pitch between the two rotors, with the upper rotor pitch angle being 1° higher than the lower one. Tinney and Valdez [30] performed experiments on a 2×2-bladed co-rotating rotor in hover at several rotational speeds and showed that the rotor thrust and sound pressure levels are more dependent on the azimuthal than on the axial separation. Interestingly, they also found that numerous rotor speed and phase angle combinations can produce the same rotor thrust, but different sound pressure levels. In a follow-up campaign Valdez and Tinney [31] employed high-speed Schlieren and particle im-

* Corresponding author.
E-mail address: e.grande@tudelft.nl (E. Grande).

https://doi.org/10.1016/j.ast.2024.109381
Received 11 November 2023; Received in revised form 11 March 2024; Accepted 8 July 2024
Available online 14 July 2024
1270-9638/© 2024 The Author(s). Published by Elsevier Masson SAS. This is an open access article under the CC BY license (http://creativecommons.org/licenses/by/4.0/).

age velocimetry to study the wake on the same rotor configuration. The main finding is that the maximum thrust coefficient corresponds to the index angle where the tip vortex from the upper rotor is located above the suction side of the lower rotor. From the mentioned studies, it appears that the azimuthal separation corresponding to the maximum thrust and minimum noise depends on various factors such as the number of rotors, axial distance, blade design and rotational speed.

Landgrebe and Bellinger [20] and Tinney and Valdez [30] conducted also experiments with different axial separations and they found that, as the axial separation increases, the thrust increases. This is probably related to a lower induced velocity at the lower rotor and a change in the blade-vortex interaction mechanism. A similar trend is obtained by Bhagwat [2], Whiteside et al. [32] and Ramasamy [24]. On the other side, the increase in thrust values corresponds to an increase in noise levels, which is in part related to an increase in loading noise.

The present work investigates the flow mechanisms affecting the thrust generation and noise emissions of two co-rotating rotor configurations in hover, made by 2x2-bladed rotors having the same axial distance but different azimuthal separation $\Delta\phi = 84°$ and 12°. Selected from Tinney's research [30], these configurations exhibit about 12.5 dB(A) difference in pressure level at the first rotor harmonic. Additionally, they are compared against isolated 2-bladed and 4-bladed rotors operating at the same conditions. The isolated rotor cases represent two extremes for the co-rotating rotors: a co-rotating configuration with zero axial separation can be seen as a single 4-bladed rotor (which has the same solidity as the co-rotating configuration), while a configuration with infinite axial separation can be seen as two 2-bladed rotors (same solidity as the upper and lower rotors of the co-rotating configuration). High-fidelity simulations are used to analyze how the mutual induction between the upper and lower rotors of the co-rotating configurations changes the evolution of the blades tip vortices and the pressure distribution on the blade surfaces with respect to the isolated rotors. This is linked to a significant difference in aerodynamic performances between upper and lower rotors. Finally, the acoustic waveforms and tonal noise emissions from the co-rotating rotors are analyzed and compared against the isolated rotor cases. The final goal is to understand if the co-rotating rotors can achieve, at the same time, higher thrust and lower tonal noise relative to the isolated (2 and 4-bladed) rotors.

The Lattice-Boltzmann/Very-Large Eddy Simulation (LB/VLES) method is employed to simulate the flow around the co-rotating geometries with $\Delta\phi = 84°$ and 12° and the single 2-bladed and 4-bladed rotors. The aerodynamic noise generation is estimated by using an acoustic analogy based on Farassat's formulation 1A of the Ffowcs-Williams and Hawkings' (FW-H) equation.

The paper is organized as follows. In Sec. 2 the computational methodology is introduced and the rotor geometry, operating conditions and computational setup are described. In Sec. 3 the numerical results are validated against experimental results. In Sec. 4 the study of the flow field around the rotor, the aerodynamic performances and the noise emission are discussed. The main findings and future work are summarized in Sec. 5.

2. Computational methodology and setup

2.1. Flow and far-field noise solver

The CFD/CAA solver Simulia PowerFLOW 6-2021, based on the Lattice-Boltzmann method (LBM), is used in this work to compute the flow around the rotor and to predict the noise generated. This software has already been validated for aerodynamic and aeroacoustic studies on large and small scale rotors [1] [7] [23]. Furthermore, the works of Romani et. [25,26] and Casalino et al. [8] show the robustness of LBM for a small-scale rotor application.

The LBM method solves the discrete form of the Boltzmann equation for the particle distribution function, which represents the probability of finding a particle at a spatial coordinate $\mathbf{x}$ and time t, while having a velocity $\mathbf{v}$. The solution of the Boltzmann equation is discretized onto a Cartesian mesh, the lattice, with an explicit time integration and collision model:

$$f_i\left(\mathbf{x} + \mathbf{v_i}\Delta t, t + \Delta t\right) - f_i\left(\mathbf{x}, t\right) = C_i\left(\mathbf{x}, t\right) \tag{1}$$

where f_i represents the particle distribution function along the i-th direction, $\mathbf{v_i}$ is the discrete particle velocity vector at the time t and position $\mathbf{x}$, $v_i\Delta t$ and Δt are the space and time velocity increments, respectively, and C_i is the collision term, modeled with the Bhatnagar-Gross-Krook (BKG) approximation [3]. The discretization used for this particular application consists of 19 discrete velocities in three dimensions (D3Q19), with a second-order Hermite expansion of the equilibrium distribution function, as needed to correctly model the first-order term of the Chapman-Enskog expansion [11] of the second-order hydrodynamic moments, which account for momentum exchange between particles due to chaotic motion [28]. The Cartesian mesh, where the Boltzmann equation is solved, is made of cubic volumetric elements (voxels). The surface of solid bodies is discretized within each voxel intersecting the wall geometry using planar surface elements (surfels). In order to simulate a rotating geometry, a ground-fixed reference frame is used in combination with a body-fixed local reference frame (LRF). The LRF is characterized by a mesh that rigidly rotates with the rotating geometry so that no relative motion between the LRF grid and the enclosed geometry occurs.

A VLES model is implemented to take into account the effect of the sub-grid unresolved scales of turbulence. Following Yakhot and Orszag [34], a two-equations $k-\epsilon$ renormalization group is used to compute a turbulent relaxation time that is added to the viscous relaxation time. To reduce the computational cost, a pressure-gradient-extended wall-model is used to approximate the no-slip boundary condition on solid walls [29,33]. The model is based on the extension of the generalized law-of-the-wall model [21] to take into account the effect of pressure gradient. These equations are iteratively solved from the first cell close to the wall in order to specify the boundary conditions of the turbulence model. For this purpose, a slip algorithm [12], obtained as a generalization of a bounce-back and specular reflection process, is used.

Far-field noise is computed by using the Ffowcs-Williams and Hawkings (FW-H) acoustic analogy applied to a permeable surface encompassing the rotors. The FW-H solver is based on a forward-time solution Casalino [6] of the formulation 1A of Farassat and Succi [14] extended to a convective wave equation [5]. This approach considers surface distributions of acoustic monopoles and dipoles, which are known as thickness and loading terms, and neglects volume distribution of quadrupoles, which accounts for all the non-linear effects (such as shock waves and turbulence mixing) in the volume surrounding the integration surface. For propellers operating at low blade-tip Mach number the quadrupole term can be neglected since the dipole noise sources, related to the tonal loading noise and broadband trailing edge noise, are dominant.

2.2. Computational setup

Two co-rotating co-axial rotors configurations (Fig. 1, first row), made by 2x2-bladed rotors, with azimuthal separations $\Delta\phi = 84°$ and 12° and a fixed axial separation $\Delta x = 2.8$ cm (0.06 D) are investigated together with isolated 2-bladed and 4-bladed rotors (Fig. 1, second row). The two co-rotating configurations are selected from Tinney's database [30] as they show a large difference in noise emission. All the rotors (co-rotating and single) have fixed-pitch APC 18x5.5 MR blades and a diameter D = 0.457 m. They operate in hover conditions with a rotational velocity of 3000 rpm, as summarized in Table 1. The blade-tip Mach number and chord-based Reynolds number based on the chord length at 75% of the blade span ($c_{75} = 3.02$ cm) are $M_t = 0.21$ and Re $= 1.1 \times 10^5$, respectively.

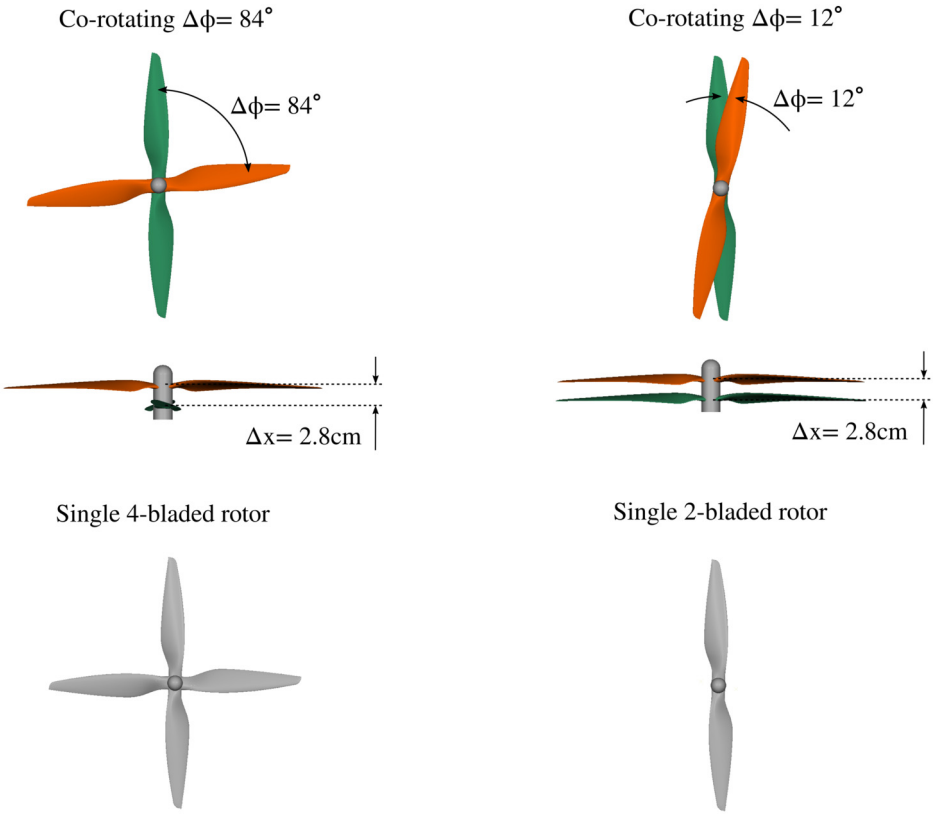

Fig. 1. Co-rotating (first row) and single (second row) rotors geometries.

Table 1
Simulated rotor configurations and operating conditions.

N	rotor type	$\Delta\phi$ [°]	Δz [cm]	V_∞ [m/s]	ω [rpm]
1	co-rotating	84	2.8	0.0	3000
2	co-rotating	12	2.8	0.0	3000
3	single 4-bladed	-	-	0.0	3000
4	single 2-bladed	-	-	0.0	3000

Table 2
Comparison between experimental and numerical thrust coefficient.

$\Delta\phi$ [°]	$c_{T_{PF}}$	$c_{T_{exp}}$	Δc_T
84	0.0915	0.104	-0.0125
12	0.0900	0.100	-0.0100

The computational fluid domain, illustrated in Fig. 2a, is a spherical volume of 185D with the co-rotating geometry at the center. Free-stream static pressure and velocity and a turbulence intensity of 0.1% of the free-stream velocity are prescribed on its outer boundary. The free-stream static pressure and velocity are set to 101.325 kPa and 0 m/sec, thus mimicking hover conditions. A total of 16 Variable Resolution (VR) regions are used to discretize the whole fluid domain, with the finest resolution regions placed around the blade leading edge and trailing edge. An additional mesh refinement is placed around the blade tips, due to their significance in capturing accurate flow physics in a rotor flow field. The smallest voxel size is 0.054 mm, resulting in $y+ \approx 15$ on the blade surface. The resulting number of fine equivalent voxels for the current study is 55 million. As sketched in Fig. 2a, an acoustic sponge, defined by two concentric spheres of $18D$ and $70D$ radius, centered around the rotor, is used to dissipate the acoustic waves and minimize the reflections from the external boundaries.

The simulation time is 0.24 sec, which corresponds to a total of 12 rotor rotations. After 2 transient rotations, results are sampled for 10 rotations. The far-field aeroacoustic analysis is performed by using the permeable formulation of the FW-H analogy. Colin et al. [13] adopted the same approach for a similar case, finding that the permeable FWH closely matched experimental results. In this study a total of 3 cylindrical surfaces (represented in red in Fig. 2a) surrounding the rotor flow field are used as permeable FWH surfaces. In order to remove spurious noise caused by the hydrodynamic fluctuations in the wake of the propeller, data are sampled on the three permeable surfaces and the pressure resulting from FWH integration over these surfaces is averaged (which is equivalent to averaging the noise signals corresponding to the three different integration surface). A similar approach is adopted by Mendez et al. [22], who also provide a mathematical expression to set the distance between the surfaces. Far-field noise is computed using the circular array of 36 microphones, sketched in Fig. 2b. The array has a radius of 3D and it is in a plane perpendicular to the rotor plane. Acoustic data are sampled at 85 kHz and pressure spectra are then calculated using a Hanning window of 50% overlap and a frequency resolution of 10 Hz.

3. Validation against experimental results

The aerodynamic and aeroacoustic results are validated against the experimental data from Tinney and Valdez [30]. The thrust coefficient, defined as $c_T = T/(\rho n^2 D^4)$ (where T is the thrust in N, ρ the air density in kg/m^3, n the propeller rotational frequency in Hz, D the propeller diameter in m), is reported in Table 2 from both simulations ($c_{T_{PF}}$) and experiments ($c_{T_{exp}}$), together with the difference between the two ($\Delta c_T = c_{T_{PF}} - c_{T_{exp}}$). The simulations underpredict the thrust coefficient by 13.6% and 11% for $\Delta\phi = 84°$ and $\Delta\phi = 12°$, respectively. The discrepancies are ascribed to the fact that the measurements were acquired during slow startup and shutdown cycles of the motor because of thermal drift due to load cell's heating from the electric motor. Moreover, the experimental uncertainty due to repeatability, found from the differ-

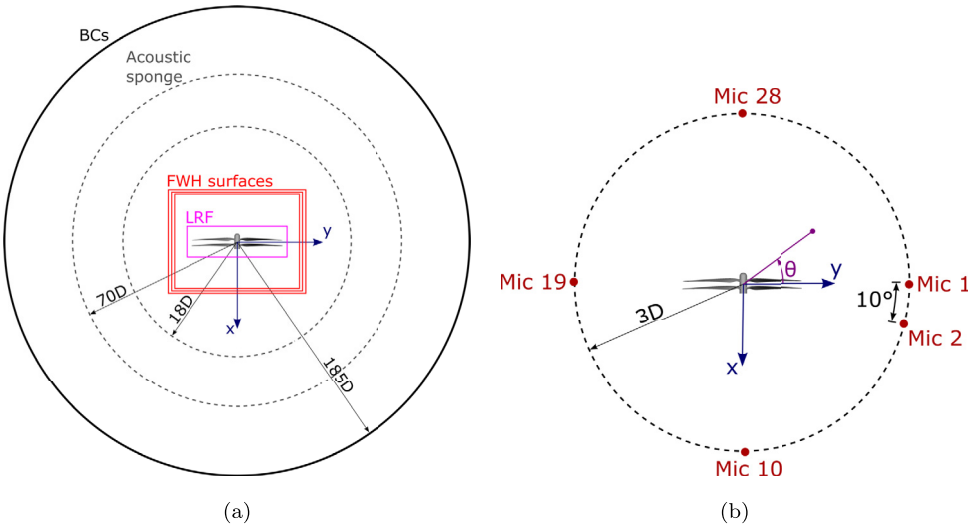

Fig. 2. Illustration of the computational setup (a). Sketch of the microphone array used for the far-field noise computation (b). (For interpretation of the colors in the figure(s), the reader is referred to the web version of this article.)

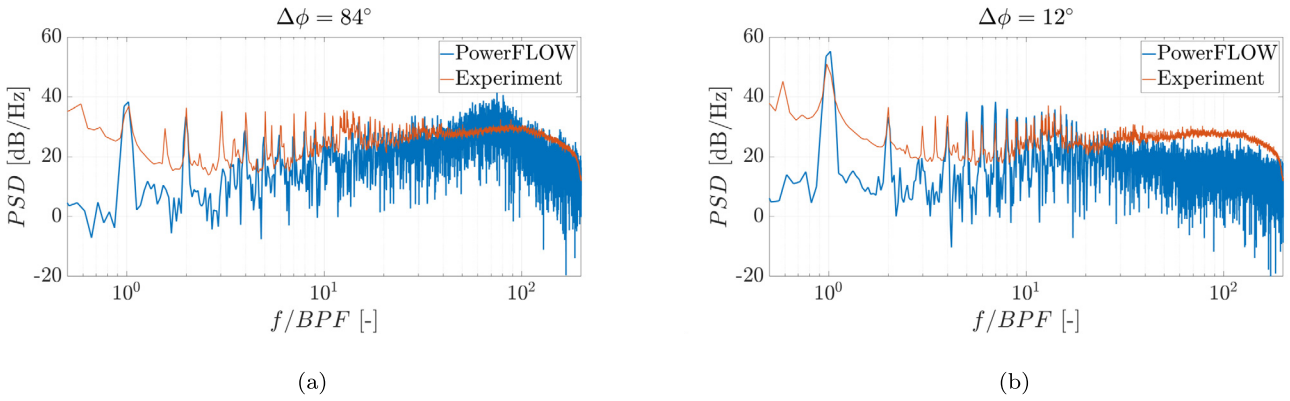

Fig. 3. Comparison between experimental and numerical far-field noise spectra at $x = 0.443$ m and $y = 0.372$ m.

ence in repeated thrust measurements of the same co-rotating configuration, is about 6% of the total thrust. From the numerical side, Casalino et al. [9] showed that the thrust increases with increasing mesh resolution for a small-scale rotor in hover at low-Reynolds numbers [15].

The far-field noise is plotted in Fig. 3 at a probe located at $x = 0.443$ m and $y = 0.372$ m. The frequency axis of each plot is normalized by the blade passing frequency BPF (100 Hz). To support the analysis of the numerical results, it is worth mentioning that the experimental spectra are affected by facility noise, responsible for the large broadband noise level at low-frequencies ($BPF < 3$), electric motor noise, causing high-frequency tones (above BPF 10) and presence of harmonics of the shaft frequency (BPF 0.5, 1.5, 2.5, etc.). The PowerFLOW spectra at BPF 1 and 2 compare reasonably well with the experimental ones, with a difference between 1.3 and 3.5 dB for both the co-rotating configurations. On the other side, the underestimation of broadband noise is expected. This is because, as shown by Romani et al. [25], a low intrusive zig-zag trip on the blade surface that guides the VLES turbulence model toward a scale resolving mode and triggers the formation of vortical structures is required for turbulent boundary layer trailing-edge noise computation. Alternatively, as shown by Casalino et al. [10], the usage of a VLES model with transitional capabilities can be made to promote the onset of turbulent fluctuation in the boundary layer (this approach would lead to an elevated computational cost, given the necessity of maintaining a y+ on the blade surface of approximately 10). Since the main focus of this work is on the effects of the azimuthal blade separation on forces and tonal noise (rather than broadband), a standard VLES model without trip is used, considering the additional effort required for a proper trip tuning.

4. Flow and acoustic analysis

This section analyzes the flow field surrounding the co-rotating rotors by showing how the mutual induction between the upper and lower rotor influences the evolution of the blade tip vortices (Sec. 4.1) and surface pressure (Sec. 4.2). The knowledge about the flow behavior is then linked to the aerodynamic performance (Sec. 4.3) and the tonal noise generation (Sec. 4.4).

4.1. Tip vortices interaction

Fig. 4 shows the iso-surfaces of λ_2, colored by velocity magnitude (in the range from 0 to 25 m/s), which highlight the trajectories of the blades tip vortices. For the co-rotating configurations, the possible interactions between the tip vortices shed from the upper and lower blades and between the tip vortices and the blades themselves are investigated. For both $\Delta\phi = 84°$ and 12°, the upper blades tip vortices are ingested deeper radially into the faster-moving region of rotor wake and, during one rotor revolution, they convect downward by about 25% of the rotor radius. Conversely, the lower blades tip vortices show a lower convection velocity into the wake with respect to the upper ones, as can be inferred from the slope of their trajectories in the direction of the rotor axis.

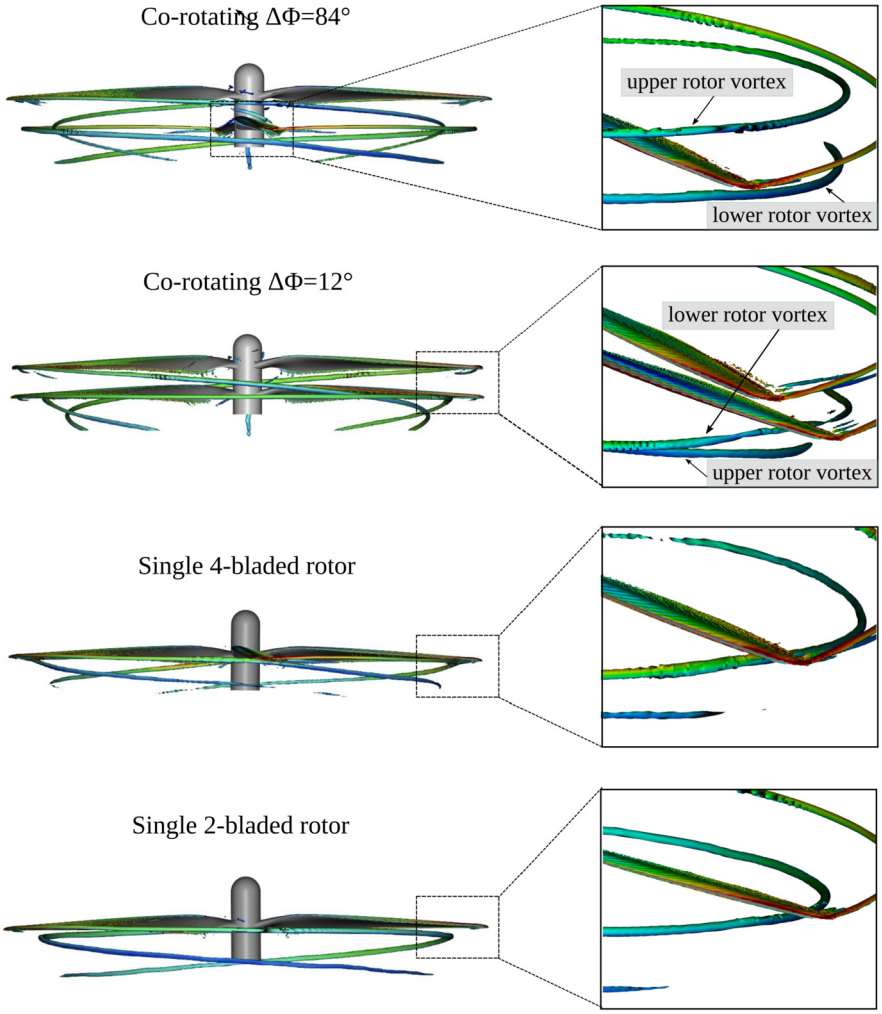

Fig. 4. Iso-surfaces of λ_2 for the co-rotating and single rotor configurations.

Fig. 5, representing the instantaneous out-of-plane vorticity ω_z, highlights the exact position of the tip vortices cores from the blade surfaces. The higher convection velocity of the tip vortices shed from the upper rotors results in a miss distance, i.e. the x-distance between the blade and tip vortex core, of 0.15R and 0.2R for $\Delta\phi = 84°$ and 12°, respectively. Conversely, the tip vortices shed from the lower blades are in close proximity to the blade surface (see also the zoom boxes in Fig. 4). Specifically, for $\Delta\phi = 84°$, the lower rotor exhibits a miss distance of 0.06R; for $\Delta\phi = 12°$, instead, the miss distance is zero, resulting in blade vortex interaction (BVI) occurring at $y/R = 0.85$. The BVI observed with the co-rotating rotors differs from the conventional helicopter BVI, where blades periodically interact with the tip vortex generated by the preceding blade. The blade-to-blade distance in stacked rotors generates a potential upwash/downwash effect created by the tip vortex vicinity to respectively the outer and inner part of the blade. Despite not being cutting through the vortical velocity profile, we still refer to this phenomenon to as BVI, following the work of Hong et al. [17]. Nonetheless, the interaction is also characterized by a periodic component. Fig. 6a shows, for both the co-rotating configurations, the surface pressure spectra from a point located at the leading edge of the lower blades at the BVI location ($y/R = 0.85$), while Fig. 6b shows the total thrust evolution for 4 propeller rotations. The BVI for the configuration $\Delta\phi = 12°$ causes periodic surface pressure fluctuations, which translate into the harmonics visible in the left figure, and thrust fluctuations at 2/rev. On the other side, the case $\Delta\phi = 84°$ does not exhibit any substantial periodic fluctuation in both the surface pressure and thrust, due to the positive miss distance for the lower blades.

The behavior of the lower rotors is similar to the isolated rotor configurations. In particular, the single 4-bladed rotor is affected by BVI, likewise the lower rotor of the $\Delta\phi = 12°$ configuration, while for the single 2-bladed rotor, the tip vortex travels in proximity to the blade surface with a miss distance of 0.05R, similar to the lower rotor of the $\Delta\phi = 84°$ configuration.

To summarize, concerning BVI, having two rotors in hover in a co-rotating configuration is beneficial for the upper rotor. Indeed, due to the induction from the lower rotor, the tip vortices from the upper rotor are accelerated downward, avoiding BVI with the upper/lower rotor blades. On the other hand, the lower rotor shows BVI when $\Delta\phi$ decreases, behaving similarly to a single 4-bladed rotor.

4.2. Surface pressure and sectional velocity

The interaction between the induction fields created by the upper and lower rotors of the co-rotating configurations changes the pressure distribution on the surface of the blades with respect to the single rotor configurations. Fig. 7 compares the surface pressure coefficient c_p at the fixed radial station r/R = 0.6 for the upper (left side) and lower rotor (right side) against the single 2- and 4-bladed rotor cases. Solid and dashed lines represent the suction and pressure side, respectively. The c_p at a generic radial section is calculated as $c_p = (p - p_\infty)/(0.5\rho_\infty V_{R_\infty}^2)$, where p is the time-averaged surface static pressure, p_∞ and ρ_∞ are the free-stream air pressure and density, respectively and V_{R_∞} is the free-stream velocity experienced by the rotor at that specific section, defined

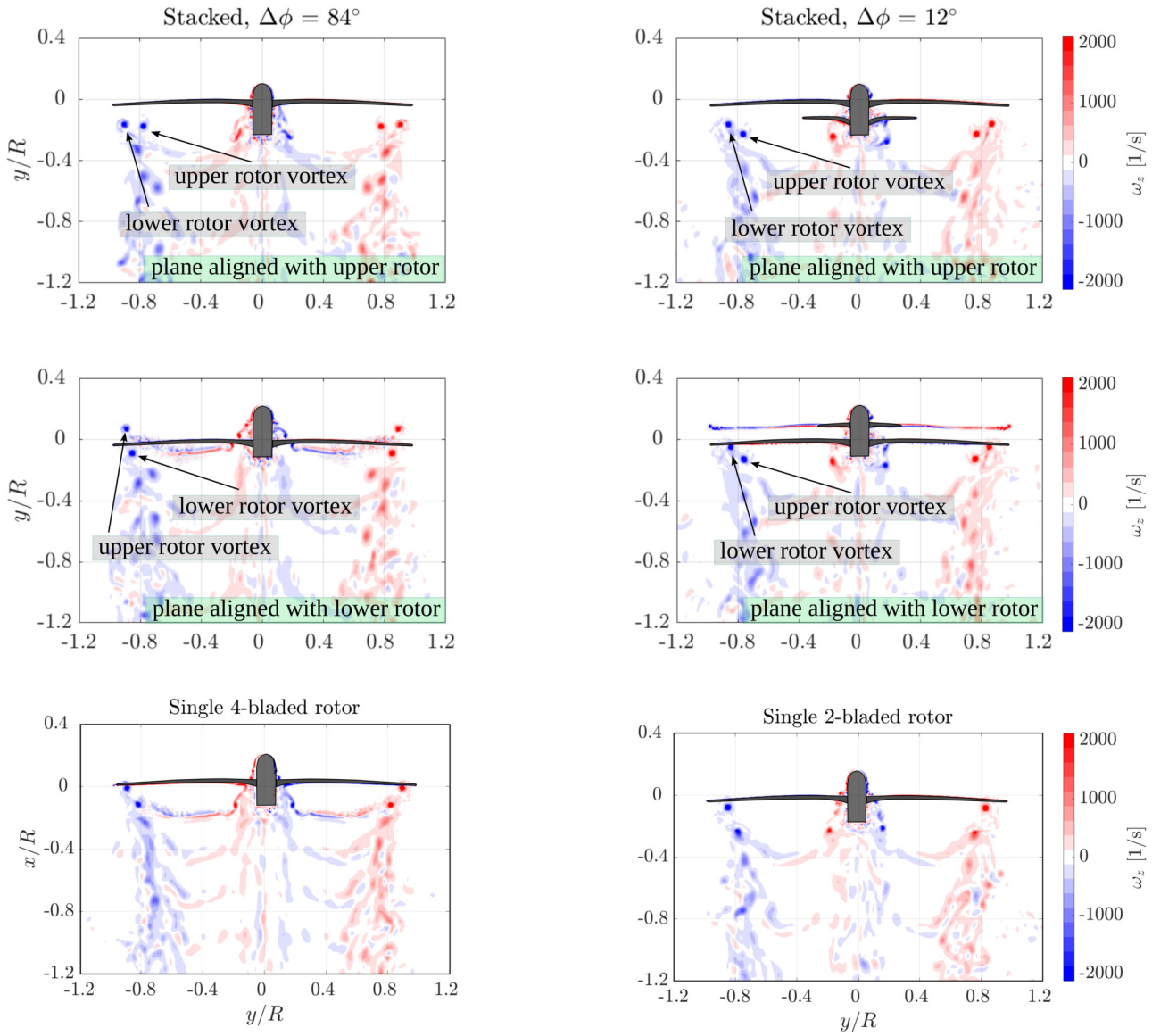

Fig. 5. Contour plot of the instantaneous vorticity in xy-planes for both co-rotating (first and second row) and single rotors (third row).

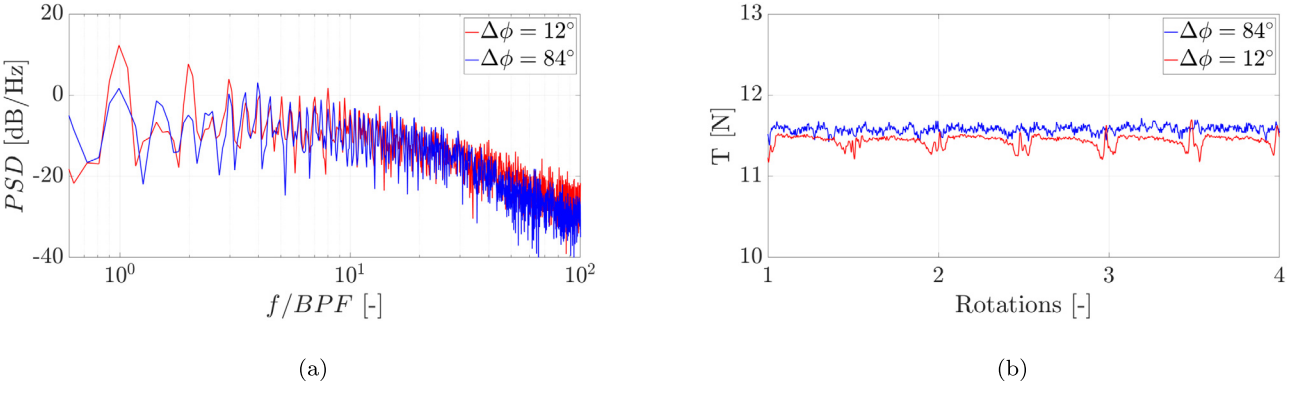

Fig. 6. Surface pressure spectra from a point on the lower rotor, at r/R = 0.85, of the co-rotating configurations (a). Total thrust evolution for four rotations (b).

as $V_{R_\infty} = \sqrt{V_\infty^2 + (\omega r)^2}$, with V_∞ being the free-stream flow velocity in m/s, ω the propeller rotational speed in rad/s and r the radial position of the blade section in m. The c_p figure is corroborated with a contour plot of the time-averaged velocity magnitude V_R (Fig. 8) around the sections at $r/R = 0.6$. Note that for $\Delta\phi = 84°$, the flow is visualized in two separate planes, one aligned with the upper blade and one with the lower blade. Conversely, for $\Delta\phi = 12°$ one unique plane aligned with the upper rotor and containing both the upper and lower blade sections, is used. The error in the in-plane velocity component due to the misalignment of the plane with respect to the lower rotor is negligible.

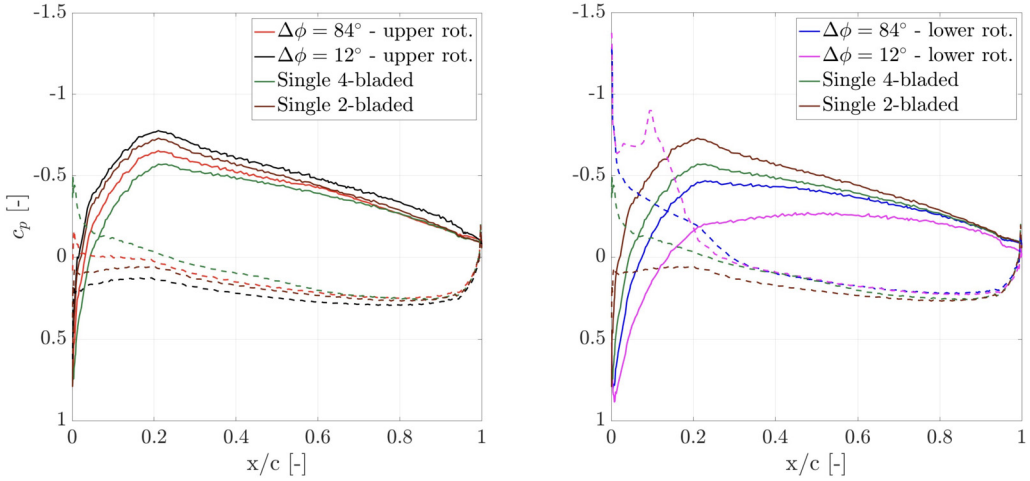

Fig. 7. Comparison of surface pressure coefficient between the co-rotating and single rotors at r/R = 0.6. Solid and dashed lines represent suction and pressure side, respectively.

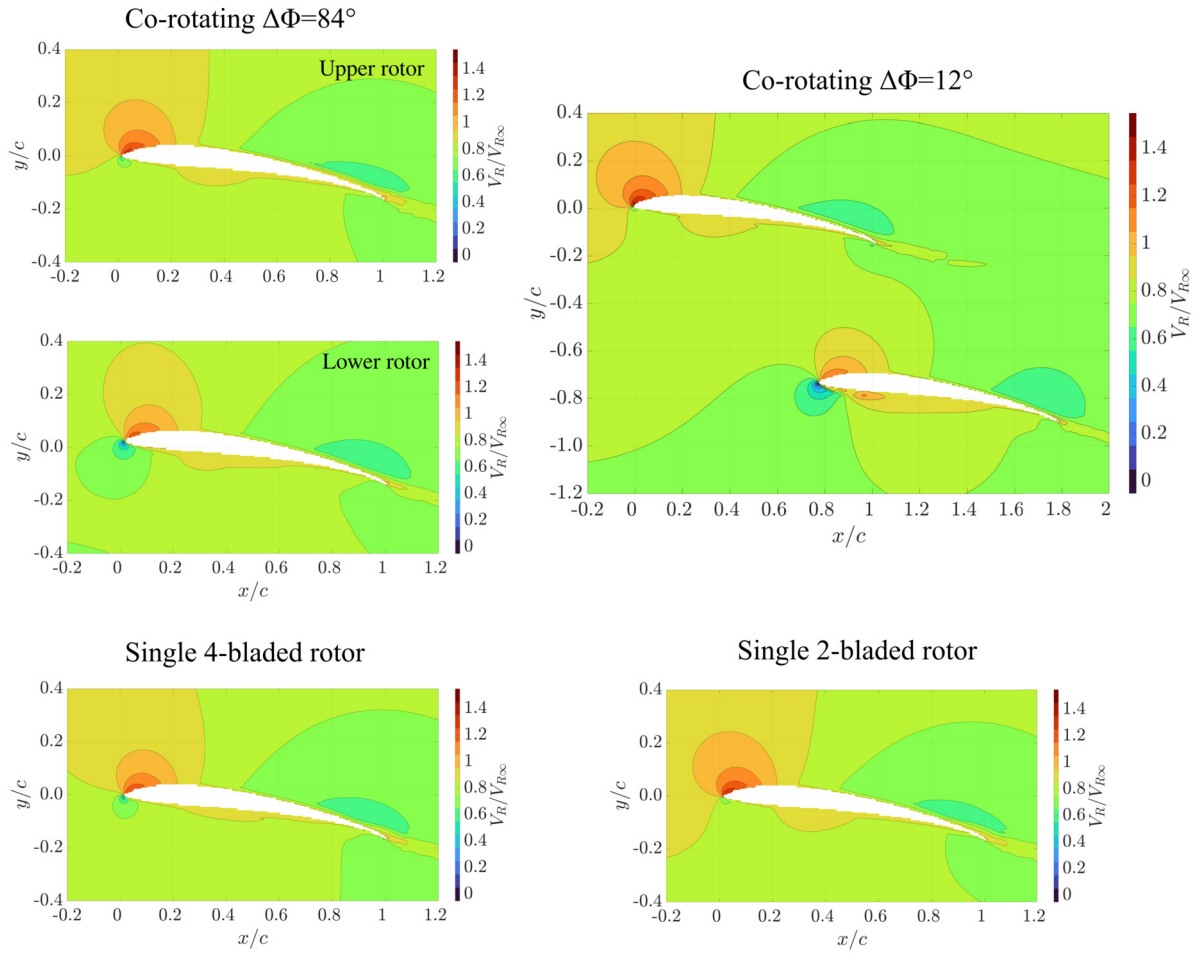

Fig. 8. Mean velocity field around the blade cross-sections at $r/R = 0.6$ for both co-rotating (first row) and single rotor (second row) configurations.

For the upper rotor (Fig. 7 left), the c_p for the co-rotating configuration with $\Delta\phi = 12°$ is the highest one. In particular, the c_p for $\Delta\phi = 12°$ shows a significant difference with respect to $\Delta\phi = 84°$ and the single 4-bladed rotor (which appears to be the lowest one). On the other hand, the c_p for $\Delta\phi = 84°$ is only higher than the single 4-bladed rotor. The analysis of the flow around the blade sections in Fig. 8 proves that for $\Delta\phi = 12°$ the lower blade, being in proximity of the upper one, behaves as a wing flap, increasing the suction (or decreasing the pressure) on the upper blade to values slightly higher than the single 2-bladed rotor.

The differences between the co-rotating and isolated cases are amplified at the lower rotor (Fig. 7 right), where both the single rotor cases show higher c_p compared to the co-rotating ones. The configuration $\Delta\phi = 12°$ exhibits the lowest c_p and hence poor aerodynamic performances. Furthermore, the co-rotating rotors show a negative c_p peak located at the pressure side (dashed line in the figure), which is asso-

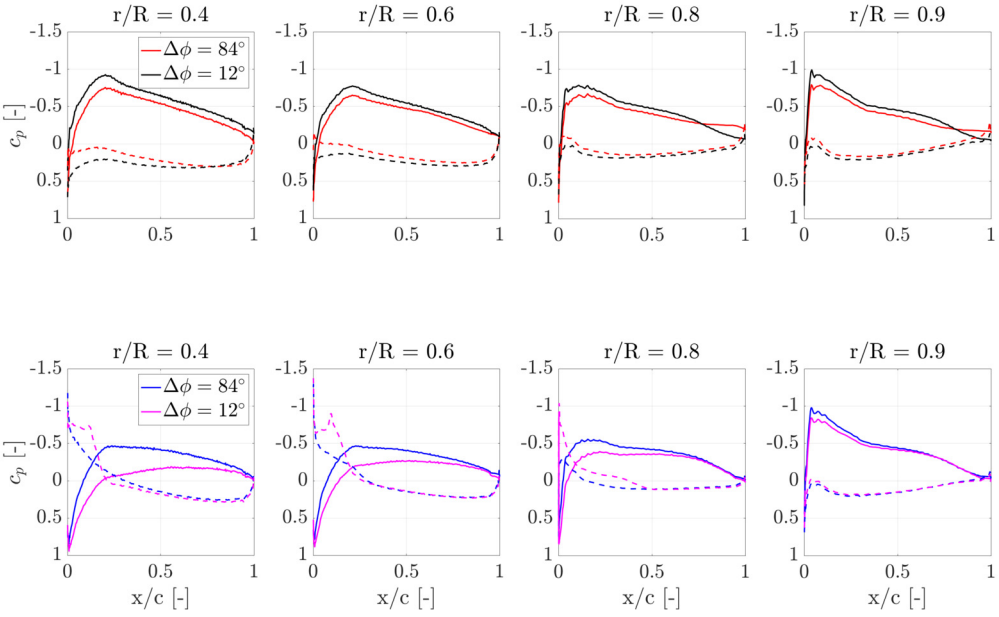

Fig. 9. Comparison of surface pressure coefficient for the upper (first row) and lower rotor (second row) at different radial stations between the co-rotating configurations $\Delta\phi = 84°$ and 12°. Solid and dashed lines represent suction and pressure side, respectively.

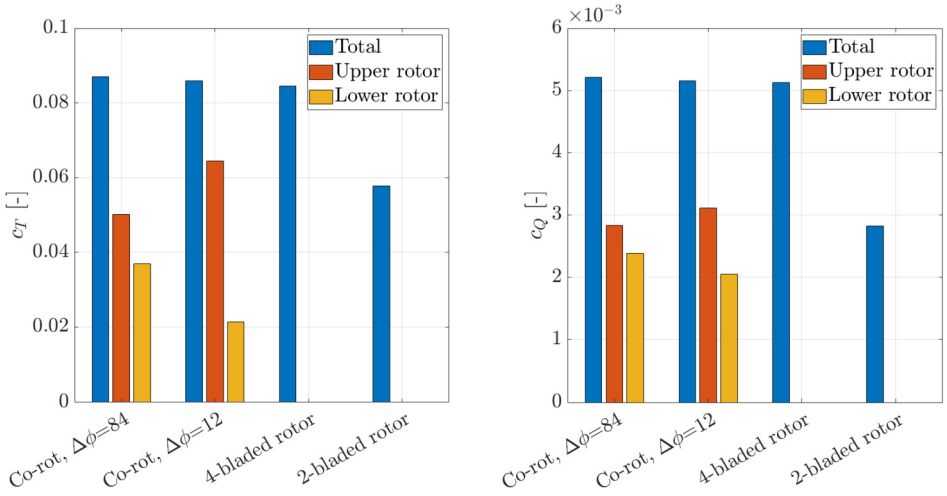

Fig. 10. Comparison of total thrust and torque between the two co-rotating configuration with $\Delta\phi = 84°$ and 12° and the single 4-bladed and 2-bladed rotors.

ciated with a negative angle of attack. This is due to the fact that the lower rotor, operating into the wake of the upper one, experiences a higher axial velocity that decreases the angle of attack. As expected, the flow analysis shows a reduced suction on the lower sections of the co-rotating cases relative to the isolated rotors. In particular, for $\Delta\phi = 12°$, as a counterpart of the flap effect (mentioned above), the upper section produces a substantial decrease in velocity on the lower one (mainly at the leading edge).

Fig. 9 compares the surface pressure coefficient c_p between the two co-rotating cases at different radial stations (ranging from $r/R = 0.4$ to 0.9). The first row of the figure shows that the c_p of the upper rotor for the 12° configuration is higher at all the radial stations. At the lower rotor instead (second row of the figure), the c_p exhibits the opposite trend, i.e. it is considerably lower for $\Delta\phi = 12°$ up to $r/R = 0.8$. This is a direct consequence of the higher c_p at the upper rotor. At the lower blade, the pressure plateau that follows the c_p peak, visible until $r/R = 0.6$ for $\Delta\phi = 12°$ and, to a minor extent, also for $\Delta\phi = 84°$, is linked to flow separation [35,4]. Finally, the vicinity of the tip vortex to the blade surface (discussed in Sect. 4.1) is responsible for the increase of c_p at $r/R = 0.9$. Indeed, the tip vortex induces an upward velocity on the outboard part of the blade, increasing the local angle of attack.

4.3. Aerodynamic performance

The induction discussed above strongly affects the aerodynamic performance of the co-rotating rotors. To assess this, the thrust c_T and torque c_Q coefficients of the co-rotating configurations are calculated and compared against the isolated 2-bladed and 4-bladed rotors.

The c_T for both co-rotating and single rotors is represented in the bar plot in Fig. 10 (left). Overall, the total c_T (defined in Sect 3) for the configurations $\Delta\phi = 84°$ and 12° is, respectively, 2.8% and 1.5% higher than the single 4-bladed rotor. The analysis of the thrust produced by the upper and lower rotors, taken individually, shows that, for both $\Delta\phi = 84°$ and 12°, the c_T of the upper rotor is higher than the lower one. This thrust imbalance is a direct consequence of the c_p distributions observed in Sect. 4.2. For $\Delta\phi = 12°$, because of the lower rotor behaving as a wing flap, the upper rotor generates 11.4% more thrust than the single 2-bladed rotor. In this case, the increased upper rotor thrust induces more

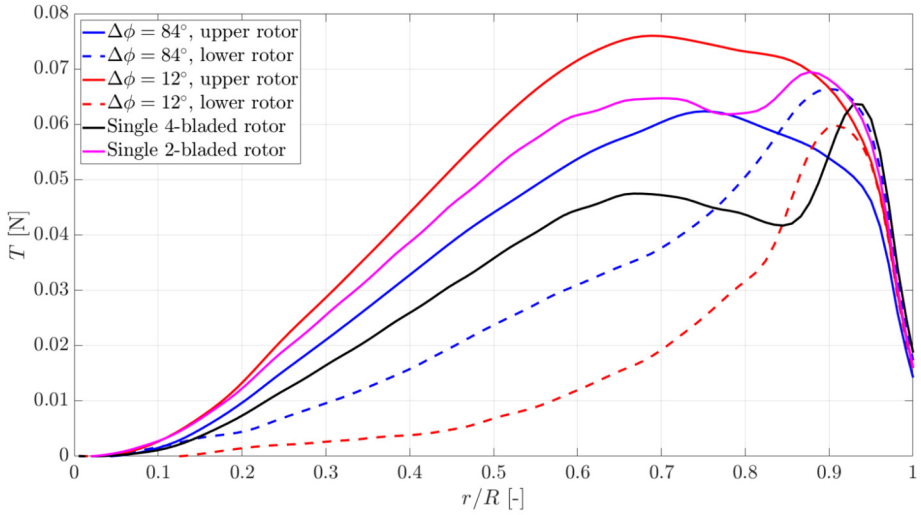

Fig. 11. Comparison of spanwise distribution of thrust between the two co-rotating configuration with $\Delta\phi = 84°$ and 12° and the single 4-bladed and 2-bladed rotors.

Table 3
Thrust variation between upper/lower rotor of the co-rotating configurations and the single 2-bladed rotor.

$\Delta\phi$ [°]	Upper rotor	Lower rotor
84	-13.0%	-36.4%
12	+11.4%	-63.0%

axial velocity at the lower rotor, thus decreasing the thrust of the latter to lower values with respect to $\Delta\phi = 84°$. The analysis of the torque coefficient, defined as $c_Q = Q/(\rho n^2 D^5)$, where Q is the torque in Nm, indicates that the c_Q for the two co-rotating configurations is the same as to the single 4-bladed rotor. Additionally, in comparison to the single 2-bladed rotor, the upper rotor for $\Delta\phi = 84°$ shows the same c_Q, while for $\Delta\phi = 12°$, the c_Q is 10.7% higher. In contrast, the lower rotor, for both $\Delta\phi$, shows a reduced c_Q (with respect to the single 2-bladed case) due to their poor aerodynamic performances.

To dig more into the differences between the two configurations, the spanwise distribution of c_T is plotted in Fig. 11. The figure shows that the rotor coupling strongly affects both the amplitude and shape of the radial distribution of c_T. While the upper rotor exhibits a smooth thrust distribution, the lower rotor of both the co-rotating configurations shows a change in the thrust slope at about $r/R = 0.85$, which is the radial position identified in Sect. 4.1 where the blade tip vortex core is located. The tip vortex causes downwash at the inner part of the blade and upwash at the outboard part, locally decreasing α and consequently c_T over the former region and increasing α and c_T over the latter. This is in agreement with Hong et al. [17], who also show the higher induction velocity at the blade tip. The increase in thrust is higher for $\Delta\phi = 12°$ because the tip vortex is at the rotor plane. The comparison with the single rotors shows, for the 4-bladed one, lower c_T values with respect to the upper rotor of both co-rotating configurations and a sharp thrust peak at $r/R = 0.95$, which is associated with a stronger BVI effect. On the other hand, the c_T of the single 2-bladed rotor is higher than the upper rotor for the 84° configuration and lower of the upper rotor for the 12° configuration because the lower rotor has a positive effect on the thrust of the upper rotor, as shown in Sect. 4.2.

The differences in thrust between upper and lower rotor and the single 2-bladed rotor are reported in Table 3.

The vicinity of the tip vortex core to lower blades surface, as a first approximation, can be considered negligible in the variation of total thrust. The velocity induced by the tip vortex on the blade surface scales linearly with the distance from the vortex core, hence this effect is nearly local (as shown in Fig. 11).

4.4. Far-field noise

By using the circular array of 36 microphones sketched in Fig. 2b, it is evaluated if the co-rotating configurations can reduce the tonal noise emission with respect to the single 2-bladed and 4-bladed rotors. The tonal noise directivity for the first BPF is calculated and plotted in Fig. 12, where the two co-rotating rotors are individually compared to the single 4- and 2-bladed rotors. Note that for the two co-rotating rotors the first BPF is equal to 100 Hz, as for the single 2-bladed rotor, instead for the single 4-bladed rotor the first BPF is 200 Hz. For a meaningful comparison, the SPL of each single rotor is scaled with the thrust of the co-rotating configuration used as a comparison. The scaling is based on the assumption that the tonal noise is dominated by steady loading noise. Furthermore, the torque contribution to tonal noise is considered negligible. In light of this, the tonal noise is approximately proportional to the thrust T as $SPL \propto 20\log(T/T_{ref})$ [19].

The comparison for $\Delta\phi = 84°$ (Fig. 12, left) reveals that this configuration is overall acoustically more efficient than the single 2-bladed rotor, being about 15 dB quieter, apart around $\theta = \pm 90°$ which are the directions perpendicular to the rotor plane. Instead, with respect to the single 4-bladed rotor, it generates overall more noise (+4.5 dB at $\theta = 0°$), apart around the upstream and downstream positions. On the other hand, the tonal noise emission for the configuration $\Delta\phi = 12°$ (Fig. 12, right) is overall significantly higher than the single 4-bladed rotor (+21.5 dB at $\theta = 0°$), and it is comparable to the single 2-bladed rotor, being 1.7 dB louder. The difference in noise emission between the two co-rotating configurations is due to constructive and destructive interference between the acoustic waves radiated by the upper and lower rotors. This is shown in Fig. 13 where the acoustic pressure signals from the upper and lower rotor at Mic 1 are plotted separately, for four propeller rotations. The resulting waveforms from the upper and lower rotor, if low-pass filtered, are similar to each other but time-shifted. The time-shift correlates to the azimuthal separation as $\Delta\phi/(n \cdot 360)$, where n is the rotational speed in Hz. Consequently, for $\Delta\phi = 84°$ the acoustic waveforms are more out of phase compared to $\Delta\phi = 12°$, thus justifying the different tonal noise components. Tinney at al. [30] demonstrated that the total acoustic waveform from the co-rotating system can be estimated as a linear superposition of the contribution of the single rotors. The increased high-frequency pressure fluctuations visible at the upper rotor for $\Delta\phi = 84°$ are likely linked to the unsteadiness induced by the tip vortex shed from the upper rotor, which remains closer to the rotor disk. Specifically, in this case, the tip vortex travels above the lower rotor blades and becomes unstable at the passage of the lower blades.

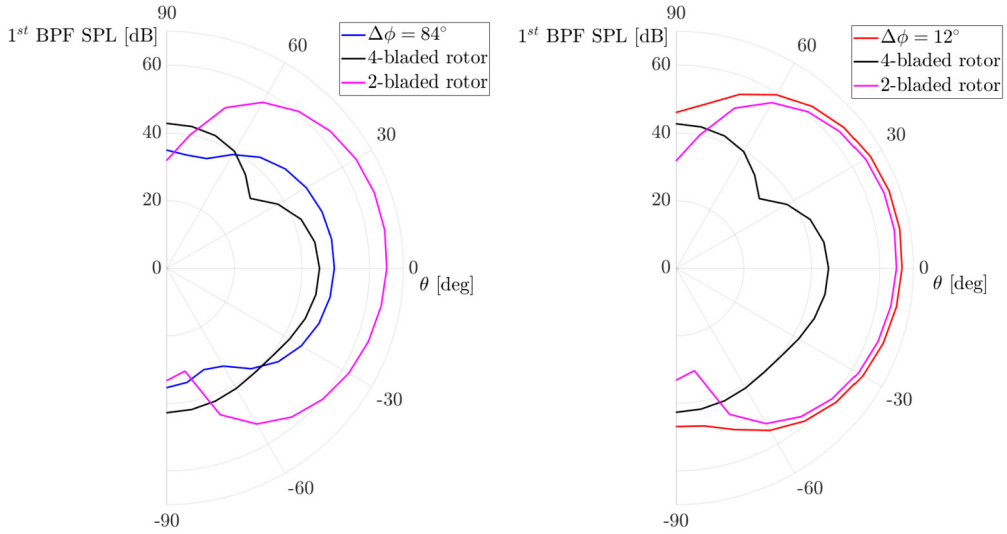

Fig. 12. Directivity of the 1^{st} BPF for the co-rotating setup $\Delta\phi = 84°$ (left) and $\Delta\phi = 12°$ (right), compared to the single 4-bladed and 2-bladed rotors.

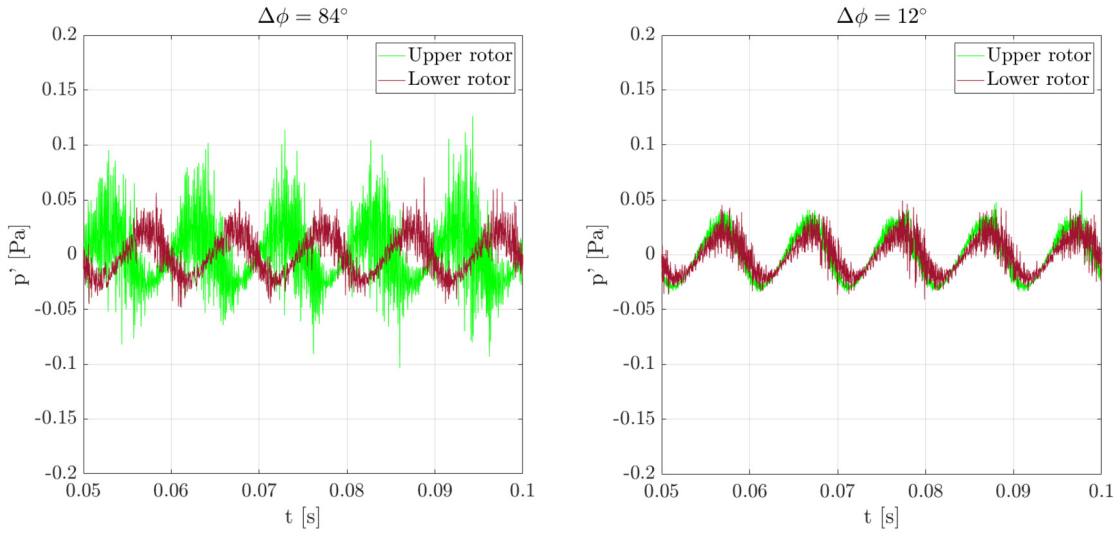

Fig. 13. Comparison between the acoustic pressure time series from the upper and lower rotors at mic 1.

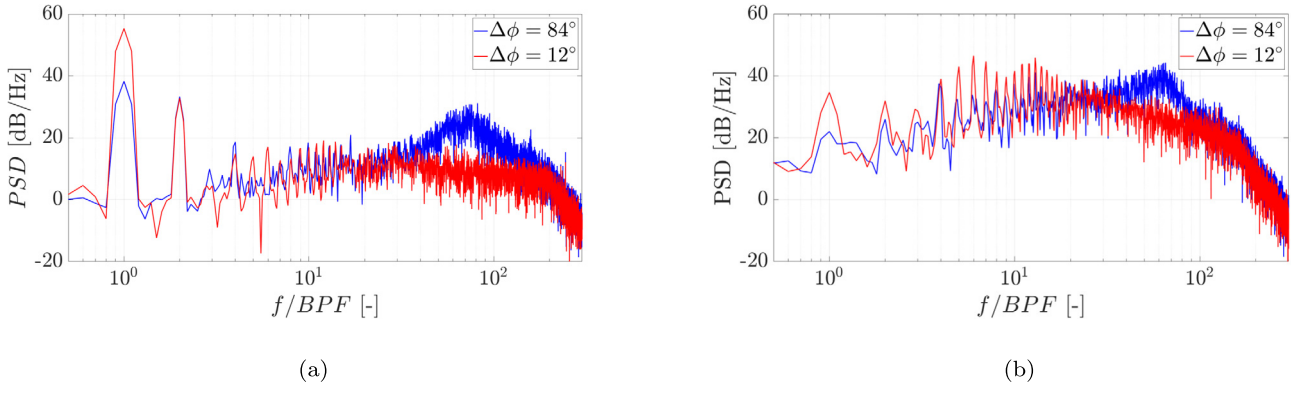

Fig. 14. Comparison of far-field noise spectra at mic 1 (a) and mic 28 (b).

Fig. 14, shows a comparison of noise spectra for the two co-rotating configurations at the rotor plane (mic 1) and upstream of the rotor plane (mic 28). At mic 1 (in-plane), the configuration $\Delta\phi = 12°$ exhibits a first BPF tone 17 dB higher with respect to $\Delta\phi = 84°$ due to destructive interference described above. At mic 28 (out-of-plane), the BPF 1 tone has a level comparable to the broadband noise, with a substantial decrease with respect to mic 1. This is expected from the loading noise directivity, which is more pronounced at the rotor plane. The difference at BPF 1 between the two configurations reduces to 13 dB. Interestingly, for $\Delta\phi = 12°$ there is a raise of high order harmonics

that is associated with unsteady pressure fluctuations caused by BVI (Sect. 4.1).

5. Conclusions

This paper presents a computational aeroacoustic study on two co-rotating rotors in hover, formed by two identical 2-bladed APC 18x5.5 MR propellers stacked on top of each other. By adopting two azimuthal separations $\Delta\phi = 84°$ and 12° between the upper and lower rotor blades and keeping the same axial separation, two different configurations are simulated and compared. In addition, isolated 2-bladed and 4-bladed rotors with the same type of blades as the co-rotating configurations are also simulated at the same conditions and used as aerodynamic and aeroacoustic reference. The lattice Boltzmann method implemented in the CFD/CAA solver Simulia PowerFLOW is used to obtain the flow solution around the rotors while the noise generation is computed by means of the Farassat's formulation 1A of the FW-H equation.

The mutual induction between upper and lower rotor of the co-rotating systems affects the evolution of the blades tip vortices and the distribution of surface pressure. For both azimuthal separations, the tip vortices from the upper rotor do not originate any BVI because it is ingested into the faster-moving region of the rotor wake and accelerated downstream. The lower blades tip vortices stagnate into a region close to the rotor plane and lead to BVI for $\Delta\phi = 12°$ at about 85% of the blade span, similarly to the isolated 4-bladed rotor. The surface pressure coefficient c_p, hence the thrust, on the upper rotor of both configurations is significantly higher than the c_p on the lower rotor since the latter, operating into the wake of the upper one, experiences a reduced angle of attack. Furthermore, for $\Delta\phi = 12°$, the lower blades act as a wing flap for the upper ones, increasing the suction and consequently the thrust of the upper rotor.

Overall, the co-rotating configurations show a total thrust increase with respect to the single 4-bladed rotor of 2.8% and 1.4% for $\Delta\phi = 84°$ and 12°, respectively. On the other side, the differences in thrust between upper and lower rotor and the single 2-bladed rotor (see Table 3) represent a quantification of the inflow interaction between upper and lower rotors. Interestingly the lower rotor for $\Delta\phi = 12°$ shows 63% of thrust reduction related to the single 2-bladed rotor.

The tonal noise emission is driven by the interference between the acoustic waveforms from the upper and lower rotor. Due to destructive interference, the configuration $\Delta\phi = 84°$ shows, at the rotor plane, a first BPF tone 15 dB lower than $\Delta\phi = 12°$, but 4.5 dB higher the single 4-bladed rotor, which is the configuration that generates overall less tonal noise.

The main issue of a co-rotating configuration is constituted by the poor aerodynamic performance of the lower rotor (especially when the azimuthal separation is decreased). A possible strategy would be to differentiate the geometry of upper and lower rotors, for instance using an upper rotor with a smaller radius than the lower one. In this way, only the inner part of the lower rotor is affected by the wake of the upper one and the outer part would work in a clean flow. However, the thrust reduction due to a smaller upper blade area must be considered. Furthermore, a positive variation of the collective pitch angle of the lower rotor would increase the angle of attack, and consequently the produced thrust. An increase in thrust for the lower rotor would be also beneficial for tonal noise reduction of configurations with azimuthal separation close to 90°. As seen in this study for $\Delta\phi = 84°$, a higher thrust would translate into a higher amplitude of the acoustic waveform from the lower rotor, thus in a more efficient destructive interference with the upper rotor waveform.

CRediT authorship contribution statement

Edoardo Grande: Data curation, Investigation, Writing – original draft, Writing – review & editing. **Shubham Shubham:** Methodology, Supervision. **Francesco Avallone:** Supervision. **Daniele Ragni:** Supervision. **Damiano Casalino:** Supervision.

Declaration of competing interest

All the authors declare that they don't have any conflicts of interest.

Data availability

Data will be made available on request.

Acknowledgements

The authors would like to thank Charles E. Tinney (University of Texas at Austin) for supplying the experimental data, and to APC Propellers for providing the propeller CAD used in this work.

References

[1] F. Avallone, L. Ende, Q. Li, D. Ragni, D. Casalino, G. Eitelberg, L. Veldhuis, Aerodynamic and aeroacoustic effects of swirl recovery vanes length, J. Aircr. (08 2019), https://doi.org/10.2514/1.C035552.
[2] M. Bhagwat, Co-rotating and counter-rotating coaxial rotor performance, in: AHS Aeromechanics Design for Transformative Vertical Flight, 2018.
[3] P.L. Bhatnagar, E.P. Gross, M. Krook, A model for collision processes in gases. I. Small amplitude processes in charged and neutral one-component systems, Phys. Rev. 94 (3) (1954) 511.
[4] M. Brendel, T. Mueller, Boundary-layer measurements on an airfoil at low Reynolds numbers, J. Aircr. 25 (1988) 612, https://doi.org/10.2514/3.45631.
[5] G. Brès, F. Pérot, D. Freed, Properties of the lattice Boltzmann method for acoustics, in: 15th AIAA/CEAS Aeroacoustics Conference (30th AIAA Aeroacoustics Conference), 2009, p. 3395.
[6] D. Casalino, An advanced time approach for acoustic analogy predictions, J. Sound Vib. 261 (4) (2003) 583–612.
[7] D. Casalino, A. Hazir, A. Mann, Turbofan broadband noise prediction using the lattice Boltzmann method, https://doi.org/10.2514/6.2016-2945, 05 2016.
[8] D. Casalino, E. Grande, G. Romani, D. Ragni, F. Avallone, Definition of a benchmark for low Reynolds number propeller aeroacoustics, Aerosp. Sci. Technol. (2021).
[9] D. Casalino, E. Grande, G. Romani, D. Ragni, F. Avallone, Towards the definition of a benchmark for low Reynolds number propeller aeroacoustics, J. Phys. Conf. Ser. 1909 (2021) 012013, IOP Publishing.
[10] D. Casalino, G. Romani, R. Zhang, H. Chen, Lattice-Boltzmann calculations of rotor aeroacoustics in transitional boundary layer regime, Aerosp. Sci. Technol. 130 (2022) 107953.
[11] H. Chen, S. Chen, W. Matthaeus, Recovery of the Navier-Stokes equations using a lattice-gas Boltzmann method, Phys. Rev. A 45 (8) (4 1992) R5339–R5342, https://doi.org/10.1103/PhysRevA.45.R5339.
[12] S. Chen, G. Doolen, Lattice Boltzmann method for fluid flows, Annu. Rev. Fluid Mech. (ISSN 0066-4189) 30 (1) (1 1998) 329–364, https://doi.org/10.1146/annurev.fluid.30.1.329.
[13] Y. Colin, B. Caruelle, A. Parry, Computational strategy for predicting cror noise at low-speed part iii: investigation of noise radiation with the Ffowcs-Williams Hawkings analogy, in: 18th AIAA/CEAS Aeroacoustics Conference (33rd AIAA Aeroacoustics Conference), 2012, p. 2223.
[14] F. Farassat, G.P. Succi, A review of propeller discrete frequency noise prediction technology with emphasis on two current methods for time domain calculations, J. Sound Vib. 71 (3) (1980) 399–419.
[15] S. Glegg, W. Devenport, Aeroacoustics of Low Mach Number Flows: Fundamentals, Analysis, and Measurement, Academic Press, 2017.
[16] J. Holden, N. Goel, Fast-forwarding to a future of on-demand urban air transportation, San Francisco, CA, 2016.
[17] Y. Hong, D. Lee, S. Yang, H. Kook, K. Yee, Exploration of stacked rotor designs for aerodynamics in hover, Aerosp. Sci. Technol. 141 (2023) 108557.
[18] G. Jacobellis, R. Singh, C. Johnson, J. Sirohi, R. McDonald, Experimental and computational investigation of stacked rotor performance in hover, Aerosp. Sci. Technol. 116 (2021) 106847.
[19] M.T. Kotwicz Herniczek, D. Feszty, S.-A. Meslioui, J. Park, F. Nitzsche, Evaluation of acoustic frequency methods for the prediction of propeller noise, AIAA J. 57 (6) (2019) 2465–2478.
[20] A.J. Landgrebe, E.D. Bellinger, Experimental investigation of model variable-geometry and ogee tip rotors (aerodynamic characteristics of variable geometry rotary wings), 1974.
[21] B. Launder, D. Spalding, The numerical computation of turbulent flows, Comput. Methods Appl. Mech. Eng. 3 (2) (3 1974) 269–289, https://doi.org/10.1016/0045-7825(74)90029-2.

[22] S. Mendez, M. Shoeybi, S. Lele, P. Moin, On the use of the Ffowcs Williams-Hawkings equation to predict far-field jet noise from large-eddy simulations, Int. J. Aeroacoust. 12 (1–2) (2013) 1–20.
[23] C. Nardari, D. Casalino, F. Polidoro, V. Coralic, P. Lew, J. Brodie, Numerical and experimental investigation of flow confinement effects on uav rotor noise, https://doi.org/10.2514/6.2019-2497, 05 2019.
[24] M. Ramasamy, Hover performance measurements toward understanding aerodynamic interference in coaxial, tandem, and tilt rotors, J. Am. Helicopter Soc. 60 (3) (2015) 1–17.
[25] G. Romani, E. Grande, F. Avallone, D. Ragni, D. Casalino, Performance and noise prediction of low-Reynolds number propellers using the lattice-Boltzmann method, Aerosp. Sci. Technol. (09 2021) 107086, https://doi.org/10.1016/j.ast.2021.107086.
[26] G. Romani, E. Grande, F. Avallone, D. Ragni, D. Casalino, Computational study of flow incidence effects on the aeroacoustics of low blade-tip Mach number propellers, Aerosp. Sci. Technol. 120 (2022) 107275.
[27] J.B. Rorke, Hover performance tests of full scale variable geometry rotors, 1976.
[28] X. Shan, X.-F. Yuan, H. Chen, Kinetic theory representation of hydrodynamics: a way beyond the Navier–Stokes equation, J. Fluid Mech. 550 (2006) 413–441, https://doi.org/10.1017/S0022112005008153.
[29] C. Teixeira, Incorporating turbulence models into the lattice-Boltzmann method, Int. J. Mod. Phys. C 09 (08) (12 1998) 1159–1175, https://doi.org/10.1142/S0129183198001060.
[30] C.E. Tinney, J. Valdez, Thrust and acoustic performance of small-scale, coaxial, corotating rotors in hover, AIAA J. (2019) 1–11.
[31] J.A. Valdez, C.E. Tinney, Wake of a coaxial corotating rotor in hover, AIAA J. 60 (8) (2022) 4829–4839, https://doi.org/10.2514/1.J061651.
[32] S. Whiteside, N. Zawodny, X. Fei, N.A. Pettingill, M.D. Patterson, P. Rothhaar, An exploration of the performance and acoustic characteristics of uav-scale stacked rotor configurations, in: AIAA Scitech 2019 Forum, 2019, p. 1071.
[33] D. Wilcox, Turbulence Modelling for CFD, third edition, DCW Industries, Incorporated, 2006.
[34] V. Yakhot, S. Orszag, Renormalization group analysis of turbulence. I. Basic theory, J. Sci. Comput. 1 (1) (1986) 3–51, https://doi.org/10.1007/BF01061452.
[35] S. Yarusevych, P. Sullivan, J. Kawall, Coherent structures in an airfoil boundary layer and wake at low Reynolds numbers, Phys. Fluids 18 (04 2006) 044101, https://doi.org/10.1063/1.2187069.

https://dspace.org/

Computational aeroacoustic study of co-rotating rotors in hover

Grande, Edoardo; Shubham, Shubham; Avallone, Francesco; Ragni, Daniele; Casalino, Damiano

2024-10-01
Elsevier
https://doi.org/10.1016/j.ast.2024.109381
Grande E, Avallone F, Ragni D, Casalino D. (2024) Computational aeroacoustic study of co-rotating rotors in hover. Aerospace Science and Technology, Volume 153, October 2024, Article number 109381

Downloaded from a DSpace repository. https://dspace.org/